Femtosecond thermionic emission from metals in the space-charge-limited regime

D. M. Riffe, X. Y. Wang, M. C. Downer, D. L. Fisher, T. Tajima, and J. L. Erskine

Department of Physics, The University of Texas, Austin, Texas 78712

R. M. More

Lawrence Livermore National Laboratory, Livermore, California 94550

Received November 7, 1992

We study femtosecond-laser-pulse-induced electron emission from W(100), Al(110), and Ag(111) in the sub-damage regime (1–44 mJ/cm^2 fluence) by simultaneously measuring the incident-light reflectivity, total electron yield, and electron-energy distribution curves of the emitted electrons. The total-yield results are compared with a space-charge-limited extension of the Richardson–Dushman equation for short-time-scale thermionic emission and with particle-in-a-cell computer simulations of femtosecond-pulsed-induced thermionic emission. Quantitative agreement between the experimental results and two calculated temperature-dependent yields is obtained and shows that the yield varies linearly with temperature beginning at a threshold electron temperature of ~0.25 eV. The particle-in-a-cell simulations also reproduce the experimental electron-energy distribution curves. Taken together, the experimental results, the theoretical calculations, and the results of the simulations indicate that thermionic emission from nonequilibrium electron heating provides the dominant source of the emitted electrons. Furthermore, the results demonstrate that a quantitative theory of space-charge-limited femtosecond-pulse-induced electron emission is possible.

PACS numbers: 78.47.+p, 79.40.+z, 79.60.Cn, 41.75.Fr.

1. INTRODUCTION

Visible-light laser-pulse excitation of a metal surface can lead to the emission of electrons through quantum excitation channels [multiphoton photoemission (MPPE)], by thermalization of the laser-pulse-excited electron gas (which leads to thermionic emission), or by a combination of these two processes, whereupon electrons in the high-energy tail of the transient thermal distribution further absorb laser photons and escape from the solid (thermally assisted photoemission). For excitation time scales longer than a few picoseconds, the local-lattice temperature T_l remains in equilibrium with the transient-electron temperature T_e.[1] Experiments with laser pulses in the nanosecond (ns) regime have demonstrated that MPPE dominates thermionic emission for incident fluences less than 40–100 mJ/cm^2.[2] Laser fluences above this level lead to a significant contribution from thermionic emission.[3,4] Experiments with picosecond (ps) laser pulses largely exhibit emission via quantum channels,[5–8] since the laser intensity is ~1000 times higher than that for ns pulses for a given fluence. In fact, for ps pulses no thermionic emission has been identified, since it appears that the damage threshold of most metal surfaces is reached before a purely thermal current can be observed, although a thermally enhanced MPPE process has been suggested for W at fluences greater than 45 mJ/cm^2, just below the onset of surface damage.[7] As excitation times cross into the sub-ps range, the dividing line in fluence between MPPE and thermally dependent emission decreases, since the electron gas becomes briefly uncoupled from the lattice, enabling T_e to become larger than T_l.[9–12] Because the specific heat of the electrons is substantially less than that of the lattice, the degree of nonequilibrium electron heating can be tremendous.[11–13] Theoretically, the dividing line between MPPE and thermionic emission has been estimated at 0.1–1 mJ/cm^2 for 100-fs pulses.[9] This estimate is supported by experiment: measurements in the region less than 0.7 mJ/cm^2 exhibit only MPPE,[14] while emission at fluences greater than 1.1 mJ/cm^2 is observed to come from nonequilibrium thermal excitation of the electron gas,[12] although whether this is due to pure thermionic emission or to thermally enhanced MPPE has not been established. Thus the dividing line between MPPE and thermionic (or thermally assisted) emission in the fs regime appears to fall within the fluence range of 0.7–1.1 mJ/cm^2, which is roughly 2 orders of magnitude less than that for ns or ps excitation.

The interpretation of laser-induced electron-emission data would be greatly simplified if space-charge effects, i.e., the Coulombic interaction among the escaping electrons, could be ignored. However, as is well known from measurements of steady-state thermionic emission,[15] the Coulombic forces of the electrons farther away from the surface tend to drive the later-escaping electrons back to the surface, producing an experimental yield often far less than that predicted by a noninteracting-particle description. Additionally, the energy distribution of the emitted electrons must necessarily be transformed by the space-charge interactions, thus obscuring the initial-energy distribution present at the metal surface.[16] Traditionally, one overcomes the space-charge suppression of the yield in steady-state thermionic emission by biasing the emitter at a negative potential with respect to a nearby anode. In this manner one can experimentally recover the theoretical yield for noninteracting particles. In laser-induced

0740-3224/93/081424-12$06.00

emission studies this approach has been adopted to attempt to surmount the space-charge suppression of the yield and thus delineate the mechanism(s) responsible for the emission from intensity-dependent yield data. As the excitation time scale becomes shorter, extraction fields must necessarily become larger for a given yield since a shorter time scale implies smaller interaction lengths for the electrons. However, even with applied fields of the order of 1000 V/cm for ns pulses,[4] 15,000 V/cm for ps pulses,[6] and 25,000 V/cm for fs pulses,[12] space-charge limiting of the yield has been evident. In the cited ns and ps studies suppression is manifest at the highest range of laser fluences used, above 125 mJ/cm^2 for the ns study and above 10–20 mJ/cm^2 for the ps studies. In the fs study of Ref. 9 suppression appears for all fluences used (1–18 mJ/cm^2). In fact, one can estimate, from the simple analytic theory presented below, that fully to overcome space-charge suppression of the yield in the fs fluence regime utilized here requires application of a field of 10^8–10^9 V/cm, a value far beyond that available in the laboratory. Clearly, then, to understand quantitatively the total yield and electron-energy distributions in the intense fs-pulse regime, one must effectively incorporate the space-charge fields of the emitted electrons.

Here we present a combined experimental, analytical theory and particle-simulation investigation of fs-pulse induced emission from Ag, Al, and W metal surfaces. Both the analytical theory and the simulation work incorporate the strong space-charge fields present in the experiment. Compared with that for longer time-scale emission,[16,17] the analytic result for the total yield is particularly simple for fs-pulse-induced emission because of the rapid spatial localization of the escaping electrons. The main result of the theory, which is confirmed by the simulations, is that the space-charge suppression of the thermionic emission produces a yield that varies linearly with temperature. For the lowest fluences the yield is dominated by surface-state enhanced multiphoton photoemission.[18] At the higher fluences quantitative agreement among results from experiment, theory, and simulation indicates that in the subdamage regime thermionic emission dominates the emission. Further, these results demonstrate that the total yield, even in the presence of strong space-charge suppression, can be useful in discerning the degree of nonequilibrium heating of the electron gas.

2. EXPERIMENTS

The W(100), Al(110), and Ag(111) samples were polished to a mirror finish by means of standard mechanical-polishing techniques before simultaneous placement in the ultrahigh-vacuum chamber. After insertion into the ultrahigh-vacuum system (base pressure $<1 \times 10^{-10}$ Torr during the experiments) and immediately preceding the experiments, the Al(110) and Ag(111) surfaces were sputtered and annealed (500–1000 eV Ar^+ ions, 700 K) until a sharp low-energy electron diffraction pattern characteristic of clean surfaces was observed. We removed major contaminants on the W(100) surface by flashing the sample to ~1800 K, which also resulted in a sharp low-energy electron diffraction pattern from this surface. For the W surface this procedure is not sufficient to remove the last monolayer of contamination; however, since our interest here is in thermionic emission, which involves the heating of the electrons over a skin depth of ~100 Å, this residual contamination was not significant for the results discussed here.

Unless otherwise stated the experimental excitation conditions were as follows. The nonequilibrium excitation of the electron gas was achieved with 10-Hz YAG-pumped, multistage amplification of 2.0-eV colliding-pulse-mode-locked laser pulses.[19] We varied the average intensity in each 90-fs pulse up to 4.9×10^{11} W/cm^2 (44 mJ/cm^2 fluence) on the sample surfaces by changing the amount of neutral-density filtration (Kodak Wratten filters) between the laser and the sample. We determined the total yield by measuring the average current through the sample to ground with a Keithley 610C solid-state electrometer. The electron-energy distributions were obtained from time-of-flight (TOF) spectra measured with a multichannel plate coupled to a transient digitizer.[20] *P*-polarized light at an angle of incidence of 66 deg was used to heat the electrons. The major and minor HWHM radii of the elliptical laser spot on the sample were $R_1 = 165$ and $R_2 = 67$ μm, respectively. All data reported here were taken with the laser intensity kept below the cumulative damage threshold of the samples. Above this threshold a dramatic increase in the yield was observed, as in the case of longer time-scale emission from surfaces.[1,7] In this paper we confine our discussion to the subdamage regime to avoid complications arising from laser-induced surface roughness and other ill-characterized processes that accompany surface damage.

Relative reflectivities of the samples were also measured as a function of the incident fluence. We obtained the relative reflectivity by splitting the laser beam into reference and sample beams. The sample beam was used to excite the samples and was reflected back out of the chamber with a dielectric mirror and focused into a Si photodiode. The reference beam was directly focused onto another Si photodiode. We kept the signal at the detectors roughly constant for all sample laser fluences by keeping the total amount of neutral-density filtration between the laser and the detectors nominally constant. More importantly, the same neutral-density filters were used in both beams. Although the absolute reflectivity r was not directly measured for any of these samples, careful measurement of another identically prepared W(100) surface with a He–Ne laser ($h\nu = 1.96$ eV) gave a reflectivity $r = 0.22 \pm 0.01$, in excellent agreement with a calculated reflectivity ratio of 0.229 ± 0.008 obtained from an average of measured optical constants from the literature.[21] We take 0.229 as the absolute value of the low-fluence W reflectivity. Intensity-dependent absolute reflectivities of the samples were thus determined from the samples' reflectivity relative to W and this low-intensity absolute value for the W(100) surface.

3. PARTICLE-IN-A-CELL SIMULATION

The computer simulations of the total yield and the electron distribution curves (EDC's) are from a modified nonrelativistic one-dimensional particle-in-a-cell (PIC) code.[22] In a conventional PIC code macroparticles are used to represent a fixed number of electrons, and space is divided

into cells of uniform size. However, in the present problem only a very small fraction of emitted electrons (approximately one in 10^6 at the highest temperatures) escapes from the near-surface region. Since the total number of macroparticles is limited by computer memory and speed to approximately 10^6, the low fractional yield causes resolution problems in both the total electron yield and the energy distributions. To overcome this difficulty we implemented several improvements over the conventional version of the code. First, we allowed different macroparticle weights for particles with different energies. Those macroelectrons with the highest energy (most likely to contribute to the final yield) were subdivided into α smaller particles, with the majority of the electrons represented by a small number of heavily weighted macroparticles. For most runs α was between 100 and 5000. Second, since the electrons encounter several different scale lengths over the total distance to the detector, the code automatically rescaled the cell size when the electrons reached the end of the grid. This rescaling took place up to eight times, with the grid spacing changing from 10^{-7} to 0.1 cm. Macroparticles were removed from the simulation when they either returned to the surface or escaped to a distance of 5 cm from the sample surface.

The one-dimensional PIC code[22] (with vacuum boundary conditions) was adapted to simulate the three-dimensional spatial geometry, with axial symmetry, through the following modifications. The surface boundary was at the center of the grid, with the image charges to the left, simulating the metal interior, and the vacuum to the right. Each macroparticle represented a disk of fixed electron charge with a radius depending on the distance the disk was from the surface. To mimic the three-dimensional interaction between charges the density of the image–charge disk was reduced according to the distance the electron-charge disk was from the surface. This density reduction has the form

$$\rho_{\text{image}} = \rho(x)\left\{1 - \frac{2x^2}{4x^2 + [R(x)]^2}\right\}, \tag{1}$$

where $\rho(x)$ is the areal charge density and $R(x)$ is the radius of the electron-charge disk created by radiation at a distance x from the surface of the metal. The form is that for the electric field on the axis of a charged disk of radius $R(x)$ and a distance $2x$ away. To model the three-dimensional free expansion of the charged disks as they travel from the surface, we assume the radius of the disk expands according to $[R(x)]^2 = x^2 + R_0^2$, where R_0 is the initial radius of the electron–charge disk at the surface. From this we get

$$\rho(x) = \rho_0 \frac{R_0^2}{x_1^2 + R_0^2}, \tag{2}$$

where $x_1 = x$ for $x < x_{\max}$ and $x_1 = x_{\max}$ for $x > x_{\max}$, where $x_{\max}$ is the radius of the metal sample. ρ_0 is the initial charge density of the disk at the surface of the metal.

The experimental laser pulse induces an approximately Gaussian radial temperature profile. However, the modified one-dimensional code can simulate only a radial step function in temperature. To incorporate the radial temperature distribution into the simulation data, we weighted several runs ranging from peak to minimum temperature according to the area of the Gaussian they represented and summed them to produce the final distribution. Macroelectrons are ejected from the surface of the metal with an energy distribution consistent with Fermi–Dirac statistics, such that the total rate is given by the standard Richardson–Dushman equation [see Eq. (7) below]. The temporal dependence of the temperature is given by the convolution of that due to the laser pulse heating and subsequent cooling of the material. The two time scales for these processes in the simulation are 100 fs for the laser pulse and 1 ps for the cooling rate for the metal. An exponential dependence for both these processes has been used for the results shown here, although this is not critical. Results using other functional forms, such as a square-wave temperature pulse assumed in the analytic model below, demonstrate that the only crucial parameter is the peak temperature attained by the heated electrons.

4. RESULTS AND DISCUSSION

A. Reflectivity

Figure 1 shows the reflectivities of the samples as functions of the incidence fluence F (average fluence inside the ellipse defined by the HWHM radii given above). Also plotted in the figure are linear fits to each data set. For all three samples there is a slight systematic change in the reflectivity as F increases. For both Ag and Al the reflectivity decreases with increasing fluence, as previously observed for these free-electron metals.[13,23,24] In the case of W the reflectivity increases slightly with fluence, which is consistent with the highly covalent nature of the element.[24] However, a sharp change in the reflectivity, which is indicative of surface damage, is not observed for any of the samples.[13,23,24] The low-fluence reflectivities

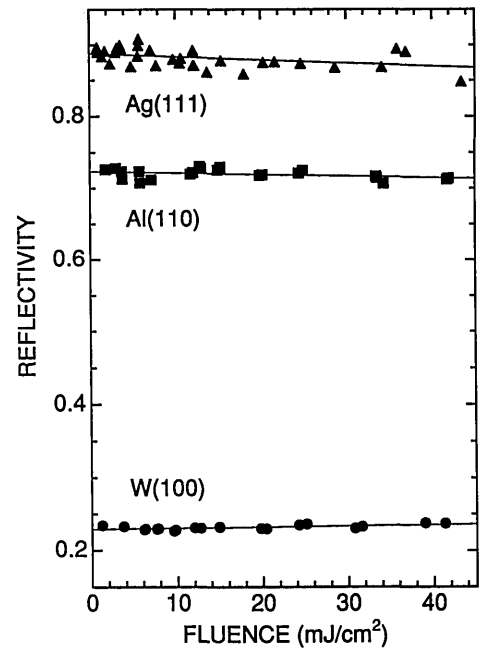

Fig. 1. Reflectivity of Ag(111), Al(110), and W(100) versus incident laser fluence.

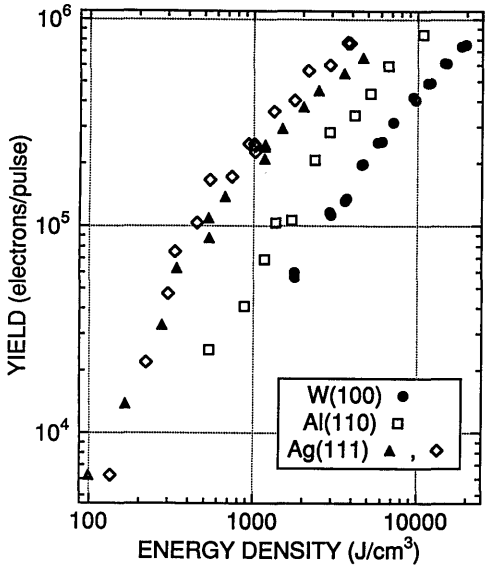

Fig. 2. Total electron yield per laser pulse versus absorbed energy density in the surface of W(100), Al(110), and Ag(111). Each type of symbol represents data from a different experimental run.

of the Al(110) and Ag(111) samples are determined from the linear fits to be 0.724 ± 0.025 and 0.887 ± 0.031, given the low-fluence W(100) reflectivity of 0.229 ± 0.008. In calculating the temperature rise of the electron gas the absorptivity of each sample is taken to be $1 - r$, where r for a given fluence is taken from the linear fits displayed in Fig. 1.

B. Total Yield

1. Experiment

In Fig. 2 the total yield is plotted versus absorbed energy density u at the surface, where $u = F(1 - r)/\delta$. Here δ is the (intensity) skin depth (122, 71, and 161 Å for Ag, Al, and W, respectively) of the metal. Note that for all energy densities the order of the yield is less than three, the minimum number of photons needed for MPPE from all three of the samples. This indicates that space-charge fields significantly suppress the yield at all laser intensities used here. For the highest intensities the yield is slightly sublinear, but for Ag and Al at the lowest intensities the yield is approximately second order. As the EDC's show below, this lowest intensity yield region is characterized by MPPE emission involving surface states.[18]

To compare the results with the theoretical and the simulation thermionic-emission calculations, the absorbed energy density is transformed to the peak temperature reached by the electron gas during excitation by the laser pulse. The peak temperature is calculated, and from standard coupled equations for the electron and lattice temperatures T_e and T_l (Ref. 9),

$$C_e(T_e)\frac{\partial T_e}{\partial t} = \kappa \Delta T_e - g(T_e - T_l) + \frac{\partial u(\mathbf{r}, t)}{\partial t}, \tag{3}$$

$$C_l(T_l)\frac{\partial T_l}{\partial t} = g(T_e - T_l). \tag{4}$$

In deriving the peak T_e, room-temperature values of the diffusion coefficient κ are used[25] (4.17, 2.37, and 1.73 W/cm K, respectively, for Ag, Al, and W), while the electron–photon coupling constant g is taken from various determinations in the literature (3.6×10^{16} for Ag,[26] 3.6×10^{17} for Al,[27] and 1.0×10^{18} W/m^3 K for W[12]). Although the values of g are somewhat uncertain, changing their magnitude by 50% results in a change in peak temperature of less than 2% for any of the metals. The lattice specific heat C_l is the Dulong–Petit value, while the electronic specific heat C_e is calculated from

$$C_e(T_e) = \int_{-\infty}^{\infty} d\epsilon\, g(\epsilon)\epsilon \frac{\partial f[\epsilon, \mu(T_e), T_e]}{\partial T_e}, \tag{5}$$

where $g(\epsilon)$ is the density of electron states at energy ϵ and $f[\epsilon, \mu(T_e), T_e]$ is the Fermi function. The chemical potential $\mu(T_e)$ is calculated from

$$n = \int_{-\infty}^{\infty} d\epsilon\, g(\epsilon) f[\epsilon, \mu(T_e), T_e], \tag{6}$$

where n is the electron density of the solid. Since the electron gas is heated only to temperatures of the order of 1 eV, core-level states can be neglected in the calculation of $g(\epsilon)$. For Al, $g(\epsilon)$ is modeled by a free-electron band with unity effective mass and three electrons per atom, which results in a filled bandwidth (Fermi energy) of 11.64 eV. For W and Ag the nd and $(n + 1)s$ conduction-band electron densities of states are modeled with a constant density of states for the d electrons and a free-electron band for the s electron.[28] The W $5d$ contribution (5 electrons/atom) to the conduction band is given a width of 11.44 eV centered at the Fermi level. Tungsten metal has one $6s$ electron/atom, whose filled bandwidth we take to be 9.50 eV, equivalent to an effective mass of 0.59. Comparison of this simplified band structure with more sophisticated theory[29] indicates that the approximation is reasonable. For Ag, parameters for the $4d$ electrons (10/atom) are taken from experimental x-ray photoemission data,[30] which reveal a $4d$ band with a width of 3.5 eV centered 5.75 eV below the Fermi level. For the Ag $5s$ electron we use the theoretical filled bandwidth of 7.66 eV (effective mass 0.79),[29] since experimentally the bottom of the s band is obscured by loss features associated with the $4d$ electrons. Calculations with different s-electron effective masses show that the results are rather insensitive to the exact value.

Figure 3 again plots the total yield from each of the samples, this time versus the peak electron temperature. The yield varies linearly with peak temperature at energies greater than ~0.30 eV, and the emission turns on at ~0.2 eV for W and Al and slightly lower for Ag. Data for W, Al, and one Ag data set (triangles) overlap quite closely. The second Ag run shown (diamonds) has a yield that is slightly higher than that of the first Ag run and is typical of run-to-run variations in yield for a given calculated temperature rise. The linear behavior of the yield with respect to peak temperature, however, is observed consistently.

2. Analytical Model

In this section we incorporate space-charge effects into a calculation of fs-pulse-induced thermionic emission from a metal surface. Additional contributions to the emission from thermally assisted MPPE can be included in the

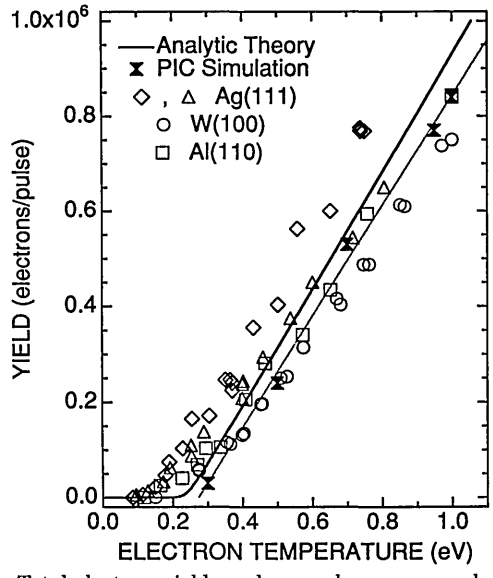

Fig. 3. Total electron yield per laser pulse versus peak electron temperature during laser heating. The open symbols are experimental data, the thicker curve is from analytic theory, and the thinner curve is a linear fit to results from simulation (filled symbols). Each type of symbol represents data from a different experimental run.

model, but to keep the following discussion as illustrative as possible we defer the inclusion of these additional terms to Subsection 4.D.

The thermionic emission rate (number/s), neglecting space-charge fields, is described by the Richardson–Dushman equation[15]

$$\frac{dN}{dt} = \pi R_0^2 C (k_B T_e)^2 \exp\left[\frac{-(E_f + e\phi - \mu)}{k_B T_e}\right], \qquad (7)$$

where k_B is the Boltzmann constant, E_f the Fermi energy, ϕ the work function of the metal, and $C = 4\pi m/h^3$, where m is the mass of the electron and h is the Planck constant. The quantity $E_f + e\phi$ is simply the potential barrier for an electron to be removed from the interior of the metal to infinity and is known as the inner potential of the metal. To extend this equation to include space-charge fields one needs to add to the inner potential an additional potential barrier that describes the effect of the space-charge fields on the electrons that escape. In general this cannot be done since the fields that the escaping electrons experience are not the same for all the electrons. However, as we show below, for fs emission the electrons that do eventually escape the solid are well localized in space at a very early time so that the fields that they experience are approximately the same. This leads to a simple expression for the added potential barrier that the escaping electrons must surmount as they leave the vicinity of the metal surface.

An expression for this added space-charge barrier can be deduced if one considers the emitted electrons while they are still just above the surface. For a short enough laser pulse the emitted electrons initially form a thin disk parallel to the surface of the solid. This is easily seen if one approximates the spatial width of the packet Δx (normal to the surface) as $(3k_B T_e/m)^{1/2}\tau$ and the lateral spatial extent as $2R_0$. For $k_B T_e = 1$ eV, $R_0 = 100$ μm, and $\tau = 1$ ps (a typical hot-electron cooling time in a solid) $\Delta x/(2R_0) = 0.004$.[31] While the packet is in the vicinity of the metal surface, i.e., at a distance $x \ll R_0$, the repulsive nature of the space-charge potential is significantly negated by the image charge of the metal, which leads to an appreciably higher density of electrons in the packet near the surface than those that eventually escape. Soon after emission from the metal surface is complete, the electrons above the surface spatially arrange themselves in the x direction according to the x component of their velocity while still maintaining a thin-disk shape parallel to the surface. This spatial arrangement occurs because of the extremely thin-disk nature of the charge distribution at the time that emission stops. Once this monotonic x-velocity–x-position condition is set up, there exists a (mathematically) connected surface (that is very planar at first) within the packet that divides the packet into those electrons that eventually escape and those that return to the metal surface. This can be seen if one considers the forces that exist on the electrons while $x \ll R_0$, as illustrated in Fig. 4. Because $x \ll R_0$, the net space-charge force on any given electron is due only to the other electrons (and their images) that are farther away from the surface, since the forces from the slower electrons are canceled by the slower electrons images. Hence the smaller the x-component of the velocity, the larger the force that acts to drive the electron back to the surface. At some x position within the packet electrons exist that will have zero velocity when they are far away from the surface. These electrons define the dividing surface within the packet—ahead of them are the electrons that escape and behind them are the electrons that return to the surface. Since the electrons that eventually escape are spatially localized in the x direction, one can justifiably consider the average potential felt by an electron in the escaping packet. Furthermore, since one can ignore

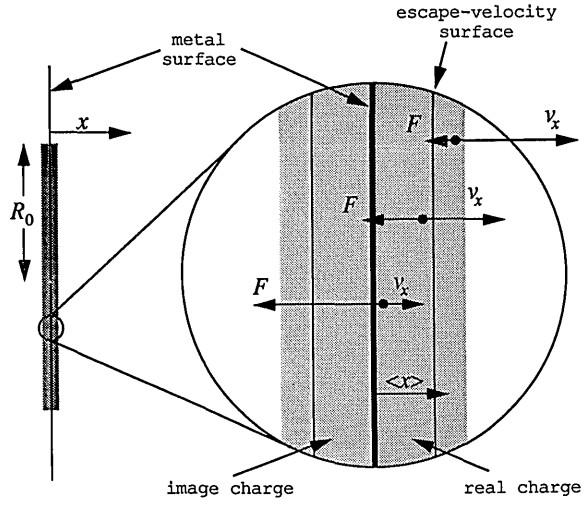

Fig. 4. Schematic representation of the dynamics of ejected electrons just after laser heating of the metal surface. The real charge is to the right of the metal surface (heavy solid line), and the image charge is to the left. Electrons at the front of the packet have the largest v_x and the smallest force acting back toward the surface. Electrons closest to the surface have the smallest v_x and the largest force acting back toward the surface. The escape-velocity surface is a mathematical surface that separates those electrons that escape from those that return to the surface.

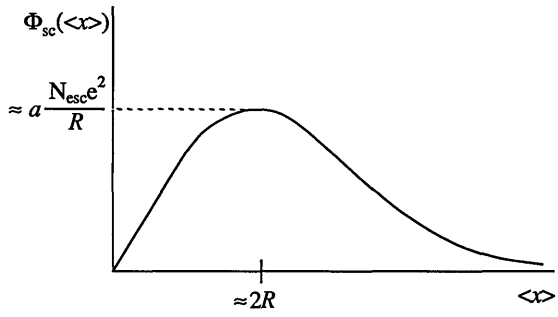

Fig. 5. Average space-charge potential experienced by electrons that escape the surface in fs-thermionic emission.

the forces from slower electrons acting on faster electrons, one can ignore the space-charge contribution from the nonescaping electrons as far as the escaping electrons are concerned. Therefore, close to the surface ($\langle x\rangle \ll R_0$, where $\langle x\rangle$ is the average value of x for the escaping electrons, the average potential energy of an electron within the packet of escaping electrons is given by

$$\Phi_{sc} \approx \frac{aN_{esc}e^2}{R_0^2}\langle x\rangle; \tag{8}$$

i.e., the space-charge potential initially builds up linearly with distance from the surface as a result of the separation of the planar escaping charge distribution and its image. N_{esc} is the number of electrons that eventually leave the near-surface region. However, the linear buildup occurs only for $\langle x\rangle \ll R_0$. Since the packet is much smaller in the normal direction, its expansion is much more rapid in that dimension than parallel to the surface. Hence the largest packet dimension is still roughly R_0 by the time the escaping electrons' image charge can be ignored (which occurs at $\langle x\rangle \approx 2R_0$). At this point the potential has increased to

$$\Phi_{sc} \approx \frac{aN_{esc}e^2}{R_0}. \tag{9}$$

Beyond this point the packet continues to expand, and the internal potential energy decreases as the electrons mutually repel one another. The average potential energy $\Phi_{sc}(\langle x\rangle)$ is sketched in Fig. 5. The constant a in relations (8) and (9) depends on the geometry of the escaping electron packet and is generally in the range of 1–2, e.g., for a uniform thin disk $a = 16/(3\pi) = 1.70$ and for a uniform sphere $a = 6/5 = 1.20$.

When we add this effective space-charge potential barrier onto the inner potential for the removal of an electron from the metal, the Richardson–Dushman rate equation for the net emission of electrons away from the surface region is thus extended to

$$\frac{dN_{esc}}{dt} = \pi R_1 R_2 C(k_B T_e)^2 \times \exp\left(-\frac{E_f - \mu + e\phi + ae^2N_{esc}/R_1}{k_B T_e}\right), \tag{10}$$

where we have now accounted for the fact that in the experiment the laser-illuminated area is elliptical. For a square-wave temperature pulse of duration τ Eq. (10) can be solved exactly to yield

$$N_{esc} = \frac{k_B T_e}{ae^2/R_1} \times \log\left[1 + C\tau\pi R_2 ae^2 k_B T_e \exp\left(-\frac{E_f - \mu + e\phi}{k_B T_e}\right)\right]. \tag{11}$$

A comparison of this equation with the Richardson–Dushman equation [Eq. (7)] yields the physically reasonable condition that, for $aN_{esc}e^2/R_1 \ll k_B T_e$, the Richardson–Dushman equation is valid, but as soon as $aN_{esc}e^2/R_1 \approx k_B T_e$ space-charge effects control the emission and produce the linear yield as a function of temperature. For temperatures below 1 eV the chemical potential μ calculated from Eq. (6) is not significantly different from $E_f = \mu(T_e = 0)$ for any of the three metals, so that the temperature dependence of μ can be neglected in this regime. Since ϕ and τ also appear inside the log function the yield is also rather insensitive to their exact values.

Also plotted in Fig. 3 is a calculated curve (thicker curve) from Eq. (11), with the following parameters: $\tau =$ 1 ps, $E_f - \mu = 0$, $\phi = 4.4$ eV, and an average value of the work functions of 4.1 eV for Al(110), 4.7 eV for W(100), and 4.5 eV for Ag(111). Here a has been set to 1.95, which is appropriate for a thin elliptical charge distribution with an eccentricity equal to that in the experiment. More-accurate values for μ and/or ϕ result in changes in the theoretical curve that are much smaller than the difference between the theory and the data. Given the simplicity of the model, the agreement with the data is gratifying. The data exhibit the linearity in the yield at the higher temperatures where the space-charge barrier controls the emission, and the magnitudes of the yields are explained to within the uncertainty in the measurements themselves. Additionally, the linear part of the data extrapolated to zero yield is within 25% of the calculated extrapolation of 0.24 eV.

The space-charge domination of the yield is clearly illustrated in Fig. 6 where, along with the experimental data

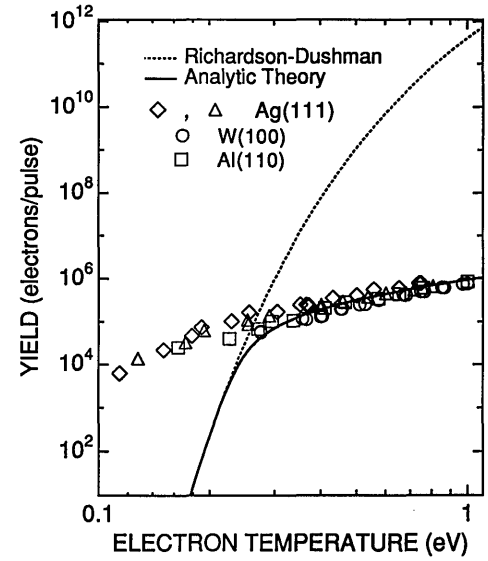

Fig. 6. Total electron yield per laser pulse versus peak electron temperature during laser heating. The open symbols are experimental data, the solid curve is from analytic theory, and the dotted curve is from the standard Richardson–Dushman formula.

and the calculated curve from Eq. (11), the standard Richardson–Dushman result neglecting the effects of space-charge is plotted. At the highest temperature of $k_B T_e = 1$ eV, the space charge allows only one in 4.2×10^5 electrons to escape. To overcome the suppression one would have to apply a potential on the sample (with respect to an anode a distance D away) of

$$V \approx -\frac{aN_{esc}e}{R_0^2}D. \tag{12}$$

That is, one must decrease the potential at a rate that is equal in magnitude but opposite in sign to the self-created barrier the electrons must climb to escape. For $k_B T_e =$ 1 eV, $R_0 = 100$ μm, and $D = 1$ mm, the potential V must be of the order of 10^7–10^8 V to negate the effects of the space charge totally. In terms of current densities, the suppression in our experiment is such that at $k_B T_e = 1$ eV a net of only ~550 A/cm^2 escapes, compared with ~2×10^8 A/cm^2 just above the surface of the metal.

Figures 5 and 6 also clearly show for the lowest temperatures that for Al and Ag the measured yield is far above that possibly due to thermionic emission; this is shown in Subsection 4.C to be due at least in part to multiphoton photoemission.

3. PIC Simulations

Computer simulation values for the total yield have been obtained and are also plotted in Fig. 3 versus the peak electron temperature. The thinner curve is a linear fit of the 5 PIC simulation results. The linear temperature dependence above a threshold of ~0.3 eV is confirmed by the computer simulations. Agreement between the PIC simulation and data is striking, especially since there are no free parameters in the computer simulations.[32] The overall agreement of the PIC simulations and the experiment with the analytic theory, in both the magnitude of the yield and its linear dependence on temperature, signifies that the analytic theory contains the essence of the space-charge suppression for fast-time-scale thermionic emission.

C. Electron Energy Distributions

1. Two-Pulse Correlation Measurements

Before we discuss in detail TOF data for single-pulse excitation, we present the results of two-pulse-correlation measurements that *prima facie* demonstrate the thermal nature of the emission in the higher fluence regime. Figure 7 displays TOF spectra for collinear, unequal-intensity two-pulse excitation of Ag(111). In this data set the trailing pulse is 25% more intense than the leading pulse. Spectra produced by either pulse alone are shown as the dotted (trailing pulse) and dashed (leading pulse) curves. When the two pulses spatially and temporally overlap, the top spectrum results. Also shown are spectra that result when the two pulses are separated by 200, 400, and 1000 fs. A clear decrease in overall emission results for longer separation of the two pulses.

That the emission depends on the temperature rise of the electron gas can be deduced if one considers the spectra for 200-, 400-, and 1000-fs separation. For these three spectra there is no temporal overlap of the two 120-fs pulses. If the emission were of a MPPE nature, then the yield would, to first order, be independent of the separation between the two pulses (for zero temporal overlap). In fact, space-charge effects would in general lead to a larger yield for greater separation, since the space-charge interaction between the two electron pulses is reduced as the pulses are temporally isolated. In the present case, however, the separation is not large enough to produce an appreciable gain in the overall yield, since space-charge effects from each electron pulse persist on the order of 100 ps.[12] On the other hand, the decreasing yield seen for increasing separation is easily understood in terms of electron heating, since the peak temperature caused by the second pulse depends on the electron temperature of the sample when the pulse arrives. The smaller the separation between the two pulses, the hotter the electrons when the second pulse arrives, and thus the greater the peak temperature. For a sufficiently long separation the sample wil have cooled by the time the second pulse arrives, so that the yield is determined solely by the second pulse, since that pulse produces a larger peak temperature than the first light pulse does. As the graph shows, significant heating from the first pulse is still evident as much as 1 ps after initial excitation of the solid. Similar conclusions on the nature of the emission have previously been reached from two-pulse-correlation total-yield measurements of W in the same fluence regime utilized here.[12] Whether the emission is due solely to thermionic emission or has a contribution from thermally assisted photoemission cannot be determined from these data. This question is discussed further in Subsection 4.D.

2. Single-Pulse Measurements

Figures 8–10 show TOF spectra recorded from each sample with increasing incident fluence on the sample surface. In Figs. 11–13 a selection of TOF spectra from Figs. 8–10 have been converted to EDC's. Common to all spectra is an increase in the high kinetic-energy cutoff of the emitted electrons with increasing temperature. Al-

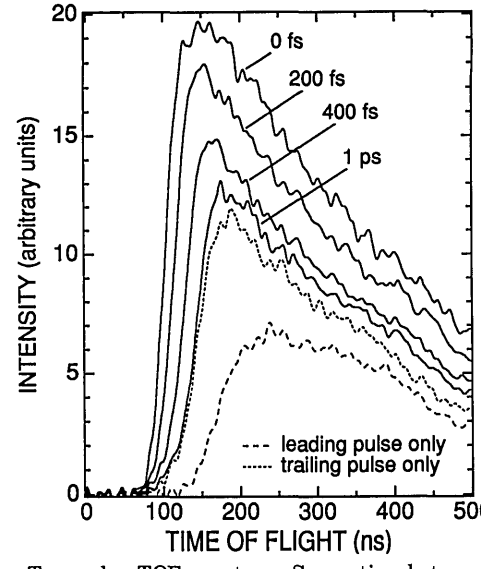

Fig. 7. Two-pulse TOF spectra. Separation between the two collinear pulses is indicated in each spectrum. The dashed and dotted spectra are obtained with only the leading or the trailing pulse, respectively, incident upon the surface.

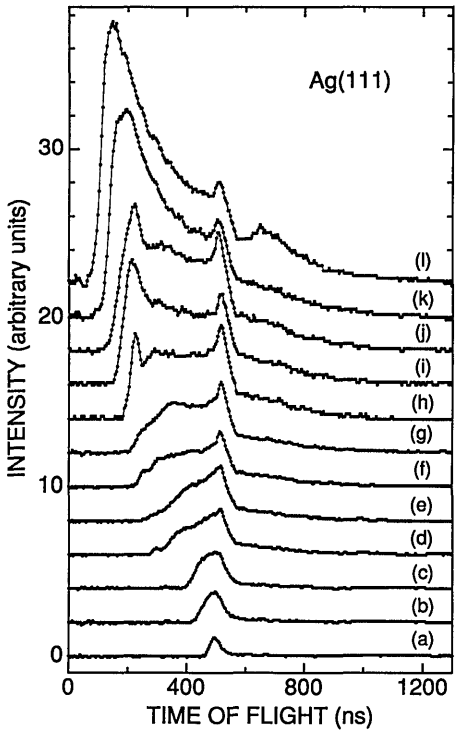

Fig. 8. TOF spectra from Ag(111). The incident fluence (mJ/cm^2) for each curve is as follows: (a) 0.90, (b) 1.5, (c) 2.4, (d) 3.2, (e) 3.5, (f) 4.8, (g) 5.8, (h) 7.8, (i) 10.5, (j) 13.7, (k) 29, (l) 37.

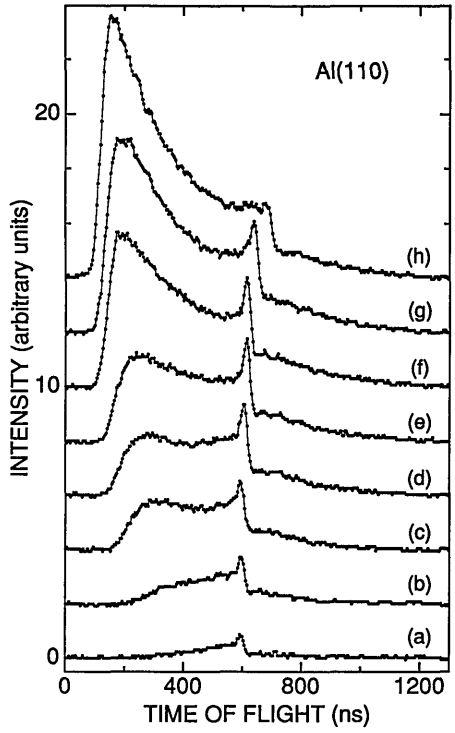

Fig. 9. TOF spectra from Ag(110). The incident fluence (mJ/cm^2) for each curve is as follows: (a) 0.87, (b) 1.5, (d) 4.7, (e) 5.4, (f) 10, (g) 15, (h) 24.

though this is not shown on these EDC's, the spectra at the highest temperatures exhibit measurable yields at kinetic energies exceeding 30 eV. Also apparent are some relatively sharp features in the spectra from each sample in the range of 400 to 600 ns. The positions, shapes, and amplitudes of these sharp features are very sensitive to the method of surface preparation and are thus associated with MPPE involving surface states.[18] The sharpness of curves (a) in Figs. 8 and 11 shows that for Ag at the lowest laser intensity the emission is entirely due to the MPPE process. This strong MPPE process in Ag accounts in part for the large total yield seen at the lowest temperatures. As the intensity is increased Figs. 8 and 10 show that the Ag spectra broaden to both lower and higher kinetic energies until the surface emission feature(s) are seen to ride on a rather large broad background characteristic of the thermionic emission regime. Figures 9 and 12 show that for the Al surface the MPPE process is relatively weaker than that for the Ag surface. Even at the lowest measurable emission currents the surface spectra sit on top of a broader background. At the highest intensities the broad part of the spectra looks remarkably like the broad part of the Ag spectra. For W the MPPE is even weaker than for the other metals. For this surface the broad thermionic background initially dominates, and it continues to do so up to the highest temperatures.

A comparison of the TOF spectra for the different samples at nearly the same peak T_e is presented in Fig. 14. The peak temperature for both W and Al is calculated to be 0.85 eV. For the Ag spectrum the calculated temperature rise is slightly lower at 0.65 eV, but the actual temperature is probably quite close to that of the W and Al spectra in the figure, since the total yield corresponding to the Ag spectrum is within 8% of the total yield corresponding to either the W spectrum or the Al spectrum. To obtain some separation of the thermal and MPPE emission in the TOF data we obtained a smooth background below the surface feature in each spectrum by fitting the monotonically decreasing sections of the TOF data away from the surface features.[33] Although slight differences exist, the broad portion of each spectrum is remarkably similar for the three metals. In Fig. 15 the TOF distributions (and the smooth background fits) of Fig. 14 have been converted to EDC's, where the similarity is even more striking. Although it is not *a priori* obvious that

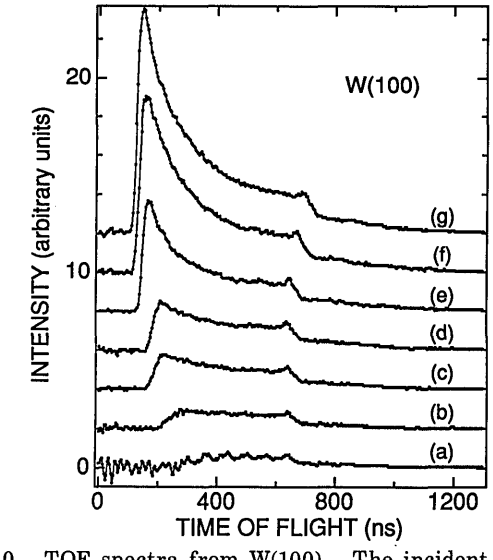

Fig. 10. TOF spectra from W(100). The incident fluence (mJ/cm^2) for each curve is as follows: (a) 3.7, (b) 6.2, (c) 9.6, (d) 12.3, (e) 20.5, (f) 31, (g) 40.

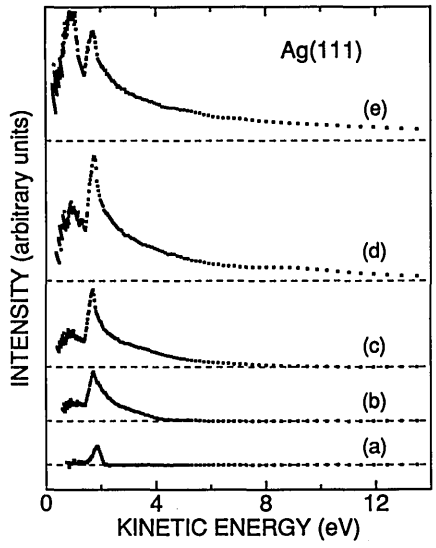

Fig. 11. EDC's from Ag(111). The incident fluence (mJ/cm^2) for each curve is as follows: (a) 0.90, (b) 3.2, (c) 5.8, (d) 13.7, (e) 37.

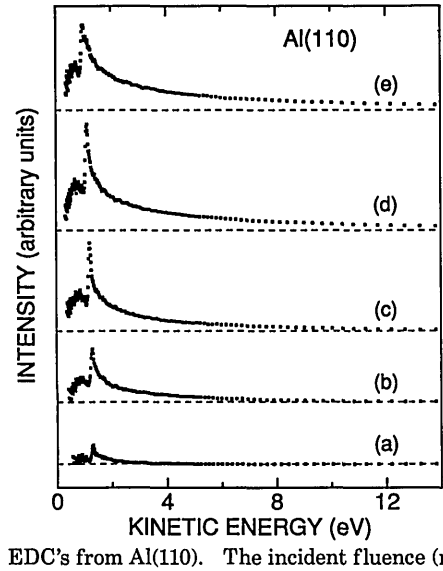

Fig. 12. EDC's from Al(110). The incident fluence (mJ/cm^2) for each curve is as follows: (a) 0.87, (b) 2.6, (c) 5.4, (d) 15, (e) 24.

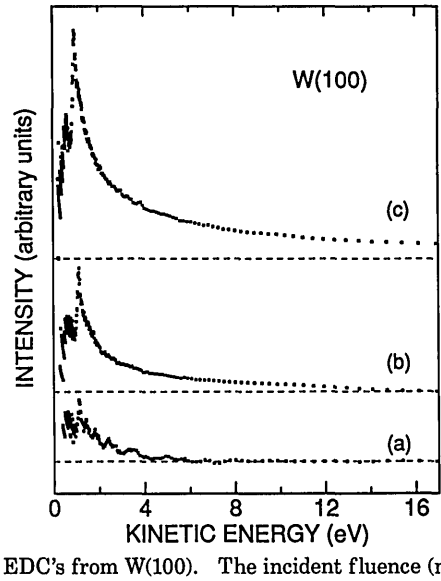

Fig. 13. EDC's from W(100). The incident fluence (mJ/cm^2) for each curve is as follows: (a) 3.7, (b) 12.3, (c) 40.

this background subtraction truly separates the MPPE and the thermionic emission contributions to the spectra, the close equivalence of the broadband spectra illustrated in Figs. 14 and 15 for all three metals suggests that this is at least a close approximation of the thermionic contribution in each curve. In fact, less well-prepared surfaces that show no evidence of surface-state emission exhibit the same broadband behavior as that illustrated in Figs. 14 and 15.

Further evidence that the separation between thermal and MPPE electrons is essentially correct is obtained by comparison with the EDC's generated from the PIC computer simulations. Simulation EDC's at 0.5, 0.7, and 0.95 eV are plotted in Fig. 16, along with W(100) data at nearly the same temperatures. Although the low-energy part of the PIC spectra shows a sharper feature than the broad thermal contribution deduced in Figs. 14 and 15 (and similarly shown in Fig. 16 for the three W data sets), the PIC EDC's mimic quite well the long tails to high kinetic energies seen in the experimental data. We emphasize that the same PIC simulations that produce this

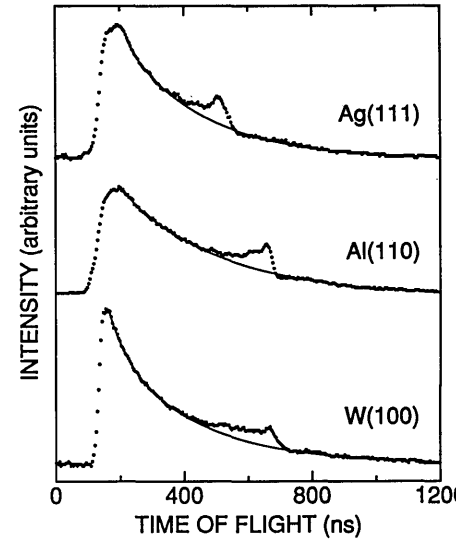

Fig. 14. Comparison of TOF spectra from W(100), Al(110), and Ag(111) for similar increases in electron temperature.

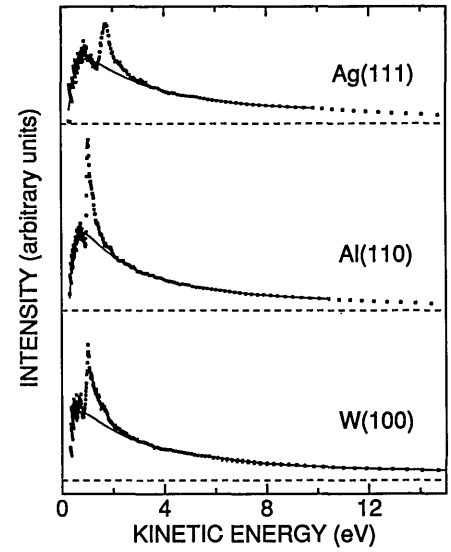

Fig. 15. EDC's obtained from TOF spectra shown in Fig. 14.

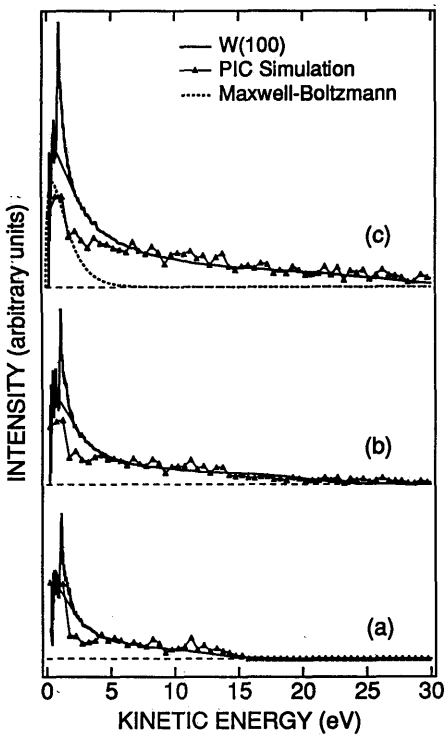

Fig. 16. Comparison of experimental EDC's from W(100) with PIC simulation EDC's at comparable peak temperatures. Experimental (simulation) peak temperatures are 0.52 (0.5), 0.68 (0.7) and 1.00 (0.95) eV for (a), (b), and (c), respectively.

agreement with the measured EDC's simultaneously explain the observed temperature-dependent total yields (Fig. 3). Also plotted in Fig. 16(c) is the spectrum our detector would measure from a Maxwell–Boltzmann distribution at an electron temperature of 1 eV in the absence of space-charge interactions. In contrast to the greater-than-30 eV electrons computed in the simulation and detected in the experiment, the Maxwell–Boltzmann distribution cuts off at roughly 8 eV for $k_B T_e = 1$ eV. The high kinetic energies measured in the EDC's are attributed to the conversion of Coulombic potential energy of the escaping packet into kinetic energy as the electrons are transported to the detector. We note that the origin of high-energy electrons seen in MPPE experiments from metal surfaces in the ps regime[34] has been similarly ascribed to the Coulombic explosion of the escaping electron packet.[16]

D. Thermally Assisted MPPE

The theory of thermally assisted photoemission, first discussed by Fowler[35] and DuBridge,[36] has since been extended to include multiphoton emission.[8] In this extended Fowler–DuBridge (EFD) theory the total emitted current is expressed as a sum of partial currents, where the first term describes standard thermionic emission (the Richardson–Dushman equation), the second is one-photon photoemission from the thermal electron distribution, the third term involves two-photon photoemission from the thermal electron distribution, and so forth. At $T = 0$ the first nonzero term must involve enough photons to excite an electron from the Fermi edge to above the vacuum level, but for any finite temperature there will be finite (although perhaps negligible) contributions from all the terms. In a 30-ps study of electron emission from W with 1.17 eV photons, for example, it was concluded that three-photon emission from a hot electron distribution supersedes four-photon MPPE at laser fluences greater than 45 mJ/cm^2.[7]

In the discussion of our results we have so far considered only the zero-photon term in the thermal contribution. The good agreement between the experiment and the two theoretical calculations appears to justify the neglect of the other terms. However, even a similarly sized contribution from other thermally activated terms[37] would be hard to discern in the present case. Because all the thermally activated partial currents in the EFD theory involve exponentials in the potential barrier divided by $k_B T_e$ {in a manner similar to the Richardson–Dushman equation [Eq. (7)]}, the effect of other partial currents, after the space-charge effect is included, is simply to add inside the argument of the log function in Eq. (11) another term for each thermally assisted partial current. When we include the thermally assisted one- and two-photon contributions in the present case, Eq. (11), for temperatures of interest here, is transformed to

$$N_{\mathrm{esc}} = \frac{k_B T_e}{ae^2/R_1} \log\left[1 + (1 + a_1 D + a_2 D^2) C\tau\pi R_2 a e^2 k_B T_e \times \exp\left(-\frac{E_f - \mu + e\phi}{k_B T_e}\right)\right], \tag{13}$$

where each parameter a_m is an effective m-photon coupling constant related to the electron escape probability and m-photon absorption cross section of the metal. The function D contains information about the laser intensity and the temperature of the electron gas and can be written as

$$D = \frac{e}{h\nu}\frac{u\delta}{\tau_1}\exp\left(\frac{h\nu}{k_B T_e}\right), \tag{14}$$

where $h\nu$ is the photon energy and τ_1 is the duration of the laser pulse. The form of Eq. (13) has two consequences. First, the linear temperature dependence in the space-charge limited regime is maintained. Furthermore, because the effect of these other thermally dependent currents is just the additional terms inside the log, even a significant partial current may do little to affect the total yield. For example, if there were another partial current with even the same amplitude as the pure thermionic emission, the total measured yield would increase by only 4.4% for space-charge limited emission. Hence the present data, in conjunction with the theory and the simulations, are consistent with some contribution from thermally assisted MPPE partial currents of magnitude comparable with that of pure thermionic emission but rule out orders-of-magnitude larger contributions from higher-order terms in the EFD theory. Since, as far as we know, there are no reliable theoretical values for the a_m's, it is in general difficult to estimate the size of these two other terms.

However, for W a comparison of the thermionic emission with the thermally assisted two-photon emission can be made, since a_2 has been experimentally determined[8] to be 2.6×10^{-26} (cm^{2}s/C)^2 at $h\nu = 2.33$. Under the assumption that a_2 is the same at $h\nu = 2$ eV and 2.33 eV we calculate the $m = 2$ contribution to the thermal current and in

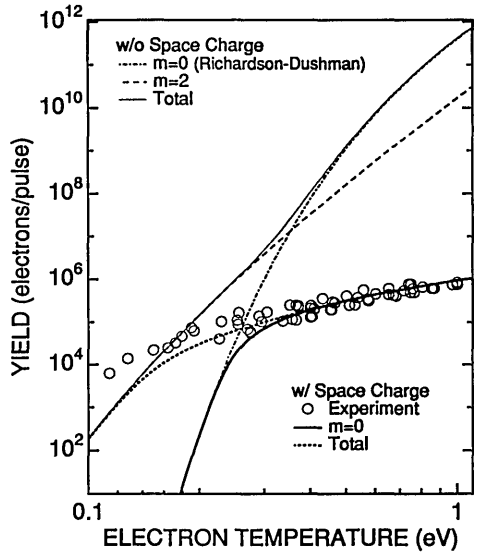

Fig. 17. Total electron yield per laser pulses versus peak electron temperature.

Fig. 17 compare it with the thermionic current. Calculated yields in the absence of space charge, which are proportional to the partial currents in the EFD theory, are plotted as dashed and dashed–dotted curves for the $m = 2$ photon and thermionic processes. A crossover at 0.3 eV is observed: below the crossover the thermally assisted $m = 2$ process dominates, while above it thermionic emission is larger. At $k_B T_e = 1$ eV current from the $m = 2$ photon process is only 4% of the purely thermal process. Figure 17 also redisplays the experimental data from Fig. 6 for all three metals (displayed as circles) as well as the space-charge-limited yield for thermionic emission (thick solid curve). When the $m = 2$ photon current is added to the thermionic current, the total yield (with space-charge interactions) is substantially increased only below 0.3 eV (dotted curve). It appears that such a term might contribute substantially to the larger yield observed below 0.2 eV. However, the lowest-temperature EDC's clearly show a sharp peak characteristic of three-photon MPPE involving surface states, not included in the analytic theory, which must therefore also contribute below 0.2 eV.

While this comparison suggests that the thermally assisted $m = 2$ photon current is larger than the thermionic current below ~0.3 eV, a recent experiment,[39] which has directly measured the internal thermalization rate of the excited electron gas in Au, provides evidence that the thermally assisted partial currents are likely negligible with fs-pulse excitation, especially at electron temperatures less than ~0.3 eV. Implicit in the discussion of these thermally assisted photoemission partial currents is the simultaneous existence of both a hot, *thermal* electron gas and photons from the laser. For a peak nonequilibrium electron temperature of 0.1 eV, internal thermalization among the excited electrons is observed to take ~700 fs, with faster times observed as the laser intensity and, hence, the resultant peak electron temperature are increased.[39] Naïvely scaling the relaxation rate for the final temperature of 0.1 eV by T_e^2 implies that at a peak electron temperature of 0.3 eV the thermalization time would be ~80 fs, which is roughly the duration of the laser pulse in our experiments. Hence, below 0.3 eV thermally assisted partial currents should be negligible since the nascently excited electrons have not yet formed a truly thermal distribution (with its long tail to high energies that provides the electrons that eventually do escape) before the laser pulse has ended. Also determined from this recent experiment is a relaxation time of ~80 fs for electrons that have kinetic energies 2.0 eV above the Fermi level, which we speculate may set a lower limit on the thermalization time of the electron gas since it appears that it may take this long to get the thermalization process started, even for higher levels of excitation. While more experimental work is needed for determination of electron-gas internal thermalization times at higher intensities, an 80-fs lower limit would imply that thermally assisted partial currents are negligible for all excitation levels used in the present experiment.

5. SUMMARY AND CONCLUSIONS

In summary, the combination of three experimental techniques: reflectivity, electron yield, and TOF energy spectrometry, along with analytic and computer simulation modeling, has permitted insight into the fs-thermionic emission process in the presence of strong space-charge fields. In contrast to emission from long laser pulses, for which complicated space-charge fields necessarily occur, the short time-scale emission with fs pulses has permitted an intuitive analytic model to be developed that does a remarkably good job of describing the total yield from the sample. Characteristic of fs thermionic or thermally assisted emission is a linear dependence on temperature for space-charge controlled emission. The predictions of the analytic model are borne out by the PIC computer simulations that have also been successful in reproducing the high-energy tails in the measured EDC's. Extensions of the analytic theory to simple quantum photoemission appear relatively straightforward and should permit further insight into ultrafast emission from solid surfaces. Furthermore, the development of analytic tools such as those reported here also offers the promise of deconvolving space-charge effects from emission physics in the more complicated higher temperature regime, where surface damage and other physical processes of extreme excitation occur.

ACKNOWLEDGMENTS

This work was supported by the U.S. Office of Naval Research (contract N00014-88-K-0663), the U.S. Air Force Office of Scientific Research (contract F4962-89-C-0444), the National Science Foundation (grants DMR-8858388 and DMR-8922359), and the Robert A. Welch Foundation (grants F-1038 and 1015).

REFERENCES AND NOTES

1. R. Yen, J. M. Liu, M. Bloembergen, T. K. Lee, J. G. Fujimoto, and M. M. Salour, Appl. Phys. Lett. **40,** 185 (1982).
2. Gy. Farkas, Zs. Naray, and P. Varga, Phys. Lett. A **24,** 134 (1967); E. M. Lofothetis and P. L. Hartman, Phys. Rev. Lett. **18,** 581 (1967).

3. Gy. Farkas, I. Kertesz, Zs. Naray, and P. Varga, Phys. Lett. A **24,** 572 (1967); E. M. Lofothetis and P. L. Hartman, Phys. Rev. **187,** 469 (1969).
4. Gy. Farkas, I. Kertez, and Zs. Naray, Phys. Lett. A **28,** 190 (1968).
5. Gy. Farkas, Gy. Horvath, I. Kertez, and G. Kiss, Nuovo Cimento Lett. **1,** 314 (1971).
6. Gy. Farkas, Gy. Horvath, and I. Kertez, Phys. Lett. A **39,** 231 (1972); L. A. Lompre, J. Thebault, and Gy. Farkas, Appl. Phys. Lett. **27,** 110 (1975).
7. J. H. Bechtel, W. L. Smith, and N. Bloembergen, Opt. Commun. **13,** 56 (1975); R. Yen, J. Liu, and N. Bloembergen, Opt. Commun. **35,** 277 (1980).
8. J. W. Bechtel, W. L. Smith, and N. Bloembergen, Phys. Rev. B **15,** 4557 (1977).
9. S. I. Anisimov, B. L. Kapeliovich, and T. L. Perel'man, Zh. Eksp. Teor. Fiz **66,** 776 (1974) [Sov. Phys. JETP **39,** 375 (1974)].
10. G. L. Easley, Phys. Rev. Lett. **51,** 2140 (1983); Phys. Rev. B **33,** 2144 (1986); H. E. Elsayed-Ali, T. B. Norris, A. M. Pessot, and G. A. Morou, Phys. Rev. Lett. **58,** 1212 (1987).
11. R. W. Schoenlein, W. Z. Lin, J. G. Fujimoto, and G. L. Easley, Phys. Rev. Lett. **58,** 1680 (1987).
12. J. G. Fujimoto, J. M. Liu, E. P. Ippen, and N. Bloembergen, Phys. Rev. Lett. **53,** 1837 (1984).
13. M. M. Milchberg, R. R. Freeman, and S. C. Davey, Phys. Rev. Lett. **61,** 2364 (1988).
14. R. B. Marcus, A. M. Weiner, J. H. Abeles, and P. S. Lin, Appl. Phys. Lett. **49,** 357 (1986); R. W. Schoenlein, J. G. Fujimoto, G. L. Easley, and T. W. Capehart, Phys. Rev. Lett. **61,** 2596 (1988).
15. See, e.g., A. C. Melissinos, *Experiment in Modern Physics* (Academic, San Diego, Calif., 1966), pp. 65–80.
16. C. Giarardeau-Montaut and J. P. Giarardeau-Montaut, Appl. Phys. Lett. **55,** 24 (1989); Phys. Rev. A **44,** 1409 (1991); T. L. Gilton, J. P. Cowin, G. D. Kubiak, and A. V. Hamza, J. Appl. Phys. **68,** 4802 (1990); M. V. Ammosov, J. Opt. Soc. Am. B **8,** 2260 (1991); G. Petite, P. Agostini, R. Trainham, E. Mevel, and P. Martin, Phys. Rev. B **45,** 12210 (1992).
17. For effects of space-charge fields on steady-state electron beams see, e.g., H. Boersch, Z. Phys. **139,** 115 (1954); B. Zimmerman, *Advanced Electron Physics* (Academic, New York, 1970); W. Knauuer, Optik **54,** 211 (1979); E. de Chambost and C. Hennion, Optik **55,** 357 (1980); J. M. J. van Leeuwen and G. H. Jansen, Optik **65,** 179 (1983).
18. K. Giesen, F. Hage, F. J. Himpsel, H. J. Riess, and W. Steinmann, Phys. Rev. Lett. **55,** 300 (1985); Phys. Rev. B **33,** 5241 (1986); W. S. Fann, R. Storz, and J. Bokor, Phys. Rev. B **44,** 10980 (1991).
19. W. M. Wood, G. Focht, and M. C. Downer, Opt. Lett. **13,** 984 (1988).
20. D. C. Anacker and J. L. Erskine, Rev. Sci. Instrum. **62,** 1246 (1991).
21. J. H. Weaver, C. Krafka, D. W. Lynch, and E. E. Kock, "Optical properties of metals, Vol. 1," in *Physics Data* (Fachinformationzentrum, Karlsuhe, West Germany, 1981), Nr 18-1, pp. 223–302.
22. T. Tajima, *Computational Plasma Physics* (Addison-Wesley, New York, 1989).
23. W. C. Banyai, D. C. Anacker, X. Y. Wang, D. H. Reitze, G. B. Focht, M. C. Downer, and J. L. Erskine, in *Ultrafast Phenomena VII,* C. B. Harris, E. P. Ippen, G. A. Mourou, and A. H. Zewail, eds. (Springer-Verlag, Berlin, 1990), p. 116.
24. X. Y. Wang and M. C. Downer, Opt. Lett. **17,** 1450 (1992).
25. G. W. C. Kaye and T. H. Laby, *Table of Physical and Chemical Constants* (Longmans, Green, London, 1966).
26. R. H. M. Groeneveld, R. Sprik, and A. Lagendijk, Phys. Rev. Lett. **64,** 784 (1990).
27. P. B. Allen, Phys. Rev. Lett. **59,** 1460 (1987).
28. W. A. Harrison, *Electronic Structure and Properties of Solids* (Dover, New York, 1989), pp. 490–500.
29. D. A. Papaconstantopolis, *Handbook of the Band Structure of Elemental Solids* (Plenum, New York, 1986).
30. S. B. DiCenzo, G. K. Wertheim, and D. N. E. Buchanan, Phys. Rev. B **33,** 5384 (1986).
31. By contrast, for ns-pulse-induced thermionic emission the results of Lofothetis and Hartman[3] on stainless steel show a transient (electron and lattice) temperature of 2800 K induced by 40-ns pulses at an intensity of 5.9×10^6 W/cm^2. For this case R_0 would have to be 7 cm for the inequality $\Delta x/(2R_0) \ll 1$ to be minimally satisfied, a spot size that is much bigger than that which can be reasonably used in the laboratory. Even if sample and chamber dimensions permitted fruitful use of such a large spot size, the energy/pulse would have to be of the order of 36 J for the temperature rise reported by Lofothetis and Hartman, a quantity not readily obtained with laboratory ns laser sources. For ps-pulse-induced MPPE emission ideas similar to the present can be used to estimate the yield; however, since there is no thermal activation in the MPPE regime, extension of the Richardson–Dushman equation is precluded, and one must use the slightly different formulation presented in Ref. 28, where the size of the space-charge barrier is set equal to the initial kinetic energy (in the direction normal to the surface) of the least energetic electrons that eventually escape. Unfortunately, unlike the model presented here the model of Ref. 28 does not simply extrapolate into the nonspace-charge-limited regime.
32. One might possibly include a multiplicative factor in the Richardson–Dushman equation [Eq. (7)] to account for less-than-perfect electron transmission through the sample interface. However, since the factor eventually ends up inside the log term in Eq. (11) it will have an inconsequential effect on the total yield in the space-charge limited regime. In both the computer simulations and the analytic theory perfect transmission has been assumed.
33. A double exponential fit of the data was used because of its simplicity and apparently reasonable interpolation of the decreasing background in the region of the MPPE features.
34. Gy. Farkas and Cs. Tóth, Phys. Rev. A **41,** 4123 (1990).
35. R. H. Fowler, Phys. Rev. **38,** 45 (1931).
36. L. A. DuBridge, Phys. Rev. **43,** 727 (1943).
37. By thermally activated terms we refer to terms identically equal to zero at 0 K. These are terms for which $mh\nu < e\phi$, where m is an integer. From the EDC's, however, it is clear that currents from these terms are dominated by the thermally activated currents above an electron temperature of ~0.3 eV.
38. H. W. K. Tom, W. S. Fann, J. Bokor, and R. H. Storz, in *Quantum Electronics and Laser Science Conference,* Vol. 13 of 1992 OSA Technical Digest Series (Optical Society of America, Washington, D.C., 1992), pp. 278–281.